SPE-173210-MS

Simulation of Coupled Thermal-Hydrological-Mechanical Phenomena in Porous and Fractured Media

P. H. Winterfeld and Yu-Shu Wu, Colorado School of Mines

This paper was prepared for presentation at the SPE Reservoir Simulation Symposium held in Houston, Texas, USA, 23–25 February 2015.

Abstract

For processes such as production from low permeability reservoirs and storage in subsurface formations, reservoir flow and the reservoir stress field are coupled and affect one another. This paper presents a thermal-hydrological-mechanical (THM) reservoir simulator that is applicable to modeling such processes. The fluid and heat flow portion of our simulator is for general multiphase, multicomponent, multi-porosity systems. The geomechanical portion consists of an equation for mean stress, derived from linear elastic theory for a thermo-poro-elastic system, and equations for stress tensor components that depend on mean stress and other variables. The integral finite-difference method is used to solve these equations. The mean stress and reservoir flow variables are solved implicitly and the remaining stress tensor components are solved for explicitly. Our simulator is verified using analytical solutions for stress and strain tensor components and is compared to published results.

Introduction

For processes such as oil and gas production from low permeability and unconsolidated reservoirs, energy production from geothermal reservoirs, and carbon dioxide storage in deep saline aquifers, an analysis of fluid and heat flow coupled with rock deformation is advantageous over one of fluid and heat flow alone because reservoir flow and the reservoir stress field affect one another.

In order to simulate such a thermal-hydrological-mechanical (THM) process, the two sets of equations, fluid and heat flow, and geomechanics, are both solved on a discretized medium. The different ways these two sets of equations can be coupled have been described by Settari and Walters (1999) and Tran *et al.* (2005). Three of these methods are iterative, explicit, and full coupling. In iterative coupling, the fluid and heat flow equations, and the geomechanical equations, are solved iteratively and sequentially until solutions for both sets converge. An example of THM processes being simulated using iterative coupling is Chin *et al.* (2002). In explicit coupling, one set of equations is solved for first and the other set is solved for next using the updated variables of the previously solved for set. Explicit coupling is a special case of iterative coupling, with only one iteration taken. An example of THM processes being simulated using explicit coupling is Minkoff *et al.* (1999). In full coupling, both sets of equations are solved simultaneously. An example of THM processes being simulated using full coupling is given by Gutierrez and Lewis (1996).

A fully coupled THM simulator was presented by Winterfeld and Wu (2014) and Hu *et al.* (2013). In their approach, the geomechanical equations relating stresses and displacements were combined to yield an equation for mean stress, a primary variable, and volumetric strain, a rock property. The computational cost of fully coupling this geomechanical formulation to the fluid and heat flow equations is relatively small since there is only one additional equation and primary variable. However, that formulation is not able to calculate the stress tensor components and information from these components, such as principal stress directions that are applicable to predicting rock failure (Jaeger *et al.* 2007), are lacking.

In this paper, we present a technique to obtain stress tensor components in the context of this mean stress geomechanical formulation. We begin by summarizing the mean stress geomechanical formulation, along with the associated fluid and heat flow formulation, and then illustrate the technique for how to obtain stress tensor components. Three example problems are then used to provide verification of our technique. The first is a comparison of simulation results to the analytical solution for displacement by a uniform load on a semi-infinite elastic medium. The second is a comparison of simulation to the analytical solution for the two-dimensional Mandel-Cryer effect. The last, a single-phase depletion problem, shows a comparison of our simulator to published results.

Fluid and Heat Flow Formulation

Our simulator's fluid and heat flow formulation is based on the TOUGH2 one (Pruess *et al.*, 1999) for general multiphase, multicomponent, multi-porosity systems. Fluid advection is described with a multiphase version of Darcy's law. Heat flow occurs by conduction and convection, the latter including sensible as well as latent heat effects. The description of thermodynamic conditions is based on the assumption of local equilibrium of all phases and rock media. The conservation equations for mass and energy can be written in differential form as:

$$\frac{\partial M^k}{\partial t} = \nabla \cdot \mathbf{F}^k + q^k \tag{1}$$

where superscript k refers to a component, M is mass per unit volume, q is source or sink per unit volume, and **F** is mass or energy flux. Mass per unit volume is a sum over phases:

$$M^k = \phi \sum_l S_l \rho_l X_l^k \tag{2}$$

where ϕ is porosity, subscript l refers to a phase, S is phase saturation, ρ is phase mass density, and X is phase mass fraction.

Energy per unit volume accounts for internal energy in rock and fluid and is the following:

$$M^{N+1} = (1-\phi) C_r \rho_r T + \phi \sum_l S_l \rho_l U_l \tag{3}$$

where ρ_r is rock density, C_r is rock specific heat, U is phase specific internal energy, and N is the number of mass components.

Advective mass flux is a sum over phases:

$$\mathbf{F}_{adv}^k = \sum_l \mathbf{F}_l X_l^k \tag{4}$$

and phase flux F_l is given by the multiphase version of Darcy's law:

$$\mathbf{F}_l = -k \frac{k_{rl} \rho_l}{\mu_l} \left(\nabla P + \nabla P_{c,l} - \rho_l \mathbf{g} \right) \tag{5}$$

where k is absolute permeability, k_r is phase relative permeability, μ is phase viscosity, P_c is phase capillary pressure, and **g** is the gravity vector. Capillary pressure is relative to a reference phase, which is the gaseous phase. Energy flux includes conductive and convective components:

$$\mathbf{F}^{N+1} = -k_t \nabla T + \sum_l h_l \mathbf{F}_l \tag{6}$$

where k_t is thermal conductivity and h is specific enthalpy.

Mean Stress Geomechanical Formulation

Our simulator's mean stress geomechanical formulation is based on the classical theory of elasticity extended to multi-porosity non-isothermal media. In the theory of elasticity, the stress-strain behavior of an isothermal elastic material is described by Hooke's law:

$$\boldsymbol{\tau} = 2G\boldsymbol{\varepsilon} + \lambda\left(tr\boldsymbol{\varepsilon}\right)\mathbf{I} \tag{7}$$

where G is shear modulus and λ is the Lamé parameter. For a thermo-poroelastic medium, a porous medium subject to changes in both temperature and stress, a pore pressure and a temperature term are added to Equation 7 (McTigue, 1986) yielding:

$$\boldsymbol{\tau} - \alpha P\mathbf{I} - 3\beta K\left(T - T_{ref}\right)\mathbf{I} = 2G\boldsymbol{\varepsilon} + \lambda\left(tr\boldsymbol{\varepsilon}\right)\mathbf{I} \tag{8}$$

where α is Biot's coefficient, T_{ref} is reference temperature for a thermally unstrained state, K is bulk modulus, and β is linear thermal expansion coefficient.

Bai *et al.* (1993) present a generalization of Hooke's law for a multi-porosity medium, a common example of which is the dual-porosity medium consisting of a network of fractures and rock matrix:

$$\boldsymbol{\tau} - \sum_j \alpha_j P_j \mathbf{I} = 2G\boldsymbol{\varepsilon} + \lambda\left(tr\boldsymbol{\varepsilon}\right)\mathbf{I} \tag{9}$$

where the summation is over multi-porosity continua. We obtain Hooke's law for a thermo-multi-poroelastic medium by including the temperature term from Equation 8 in Equation 9 for each multi-porosity continuum, since temperature varies between multi-porosity continua. We also weight each temperature term by the porous continuum volume fraction, ω_j, since the bulk modulus and linear thermal expansion coefficient describe the overall porous medium:

$$\boldsymbol{\tau} - \left[\sum_j \left(\alpha_j P_j + 3\beta K\omega_j\left(T_j - T_{ref}\right)\right)\right]\mathbf{I} = 2G\boldsymbol{\varepsilon} + \lambda\left(tr\boldsymbol{\varepsilon}\right)\mathbf{I} \tag{10}$$

Expressions for the generalized Biot's coefficients, α_j, for a dual-porosity medium have been presented by Wilson and Aifantis (1982):

$$\alpha_1 = 1 - \frac{K}{K_*} \tag{11}$$

and

$$\alpha_2 = \frac{K}{K_*}\left(1 - \frac{K_*}{K_s}\right) \tag{12}$$

where K_s is the solid modulus, K_* is the modulus of the porous medium without the fractures, subscript 1 refers to the fractures, and subscript 2 refers to the matrix.

Two other fundamental relations in the theory of linear elasticity are the relation between the strain tensor and the displacement vector **u**:

$$\boldsymbol{\varepsilon} = \frac{1}{2}\left(\nabla\mathbf{u} + \nabla\mathbf{u}^t\right) \tag{13}$$

and the static equilibrium equation:

$$\nabla \cdot \boldsymbol{\tau} + \mathbf{F}_b = 0 \tag{14}$$

where $\mathbf{F}_b$ is the body force. We combine Equations 10, 13, and 14 to obtain the thermo-multi-poroelastic Navier equation:

$$\nabla\left[\sum_j\left(\alpha_j P_j+3\beta K\omega_j T_j\right)\right]+(\lambda+G)\nabla(\nabla\cdot\mathbf{u})+G\nabla^2\mathbf{u}+\mathbf{F}_b=0 \tag{15}$$

Taking the divergence of Equation 15 yields:

$$\nabla^2\left[\sum_j\left(\alpha_j P_j+3\beta K\omega_j T_j\right)\right]+(\lambda+2G)\nabla^2(\nabla\cdot\mathbf{u})+\nabla\cdot\mathbf{F}_b=0 \tag{16}$$

The trace of the stress tensor, an invariant, is obtained from Equation 10 as:

$$K\varepsilon_v=\tau_m-\sum_j\left(\alpha_j P_j+3\beta K\omega_j\left(T_j-T_{ref}\right)\right) \tag{17}$$

where τ_m is the mean stress, the average of the normal stress tensor components, and ε_v is the volumetric strain, the sum of the normal strain components. Finally, combining Equations 16 and 17, and noting that the divergence of the displacement vector is the volumetric strain, yields an equation relating mean stress, pore pressures, and temperatures (Winterfeld and Wu, 2014):

$$\nabla\cdot\left[\frac{3(1-\upsilon)}{1+\upsilon}\nabla\tau_m+\mathbf{F}_b-\frac{2(1-2\upsilon)}{1+\upsilon}\nabla\left(\sum_j\left(\alpha_j P_j+3\beta K\omega_j T_j\right)\right)\right]=0 \tag{18}$$

where υ is Poisson's ratio.

We couple fluid and heat flow to geomechanics by solving Equation 18 along with the mass and energy conservation equations (Equation 1) from the fluid and heat flow formulation. Equation 18 is a momentum conservation equation in terms of mean stress, the primary thermodynamic variable associated with our geomechanical formulation. Volumetric strain is an additional property arising from our geomechanical formulation and is calculated from Equation 17.

Rock properties, namely porosity and permeability, are correlated to effective stress, a general definition of which was given by Biot and Willis (1957):

$$\tau'=\tau_m-\alpha P \tag{19}$$

One such correlation for porosity is based on its definition, the ratio of fluid volume to bulk volume:

$$\phi=1-\frac{V_s}{V_0\left(1-\varepsilon_v\right)} \tag{20}$$

where V_s is the solid or grain volume and V_0 is the unstrained bulk volume. Other such correlations for these properties used in our simulator appear in Winterfeld and Wu (2014).

Stress Tensor Component Formulation

In this section, we derive equations for calculation of the stress tensor components. Consider the x-component of Equation 15:

$$\frac{\partial}{\partial x}\left[h(\mathbf{P},\mathbf{T})\right]+(\lambda+G)\frac{\partial}{\partial x}(\nabla\cdot\mathbf{u})+G\nabla^2 u_x+F_{b,x}=0 \tag{21}$$

where

$$h(\mathbf{P},\mathbf{T})=\sum_j\left(\alpha_j P_j+3\beta K\omega_j\left(T_j-T_{ref}\right)\right) \tag{22}$$

Differentiating Equation 21 by x and eliminating strains and displacements in favor of stresses using Equations 10, 13, and 17 yields an equation relating the xx-normal stress component, mean stress, pore pressures, and temperatures:

$$\frac{\partial^2}{\partial x^2}\left[h(\mathbf{P},\mathbf{T})\right]+\frac{3}{2(1+\upsilon)}\frac{\partial^2}{\partial x^2}\left(\tau_m-h(\mathbf{P},\mathbf{T})\right)+\frac{1}{2}\nabla^2\left(\tau_{xx}-h(\mathbf{P},\mathbf{T})-\frac{3\upsilon}{1+\upsilon}\left(\tau_m-h(\mathbf{P},\mathbf{T})\right)\right)+\frac{\partial}{\partial x}F_{b,x}=0 \tag{23}$$

Repeating this procedure for the y- and z-components of Equation 15 yield similar equations for the yy- and zz-normal stress components:

$$\frac{\partial^2}{\partial y^2}\left[h(\mathbf{P},\mathbf{T})\right]+\frac{3}{2(1+\upsilon)}\frac{\partial^2}{\partial y^2}\left(\tau_m-h(\mathbf{P},\mathbf{T})\right)+\frac{1}{2}\nabla^2\left(\tau_{yy}-h(\mathbf{P},\mathbf{T})-\frac{3\upsilon}{1+\upsilon}\left(\tau_m-h(\mathbf{P},\mathbf{T})\right)\right)+\frac{\partial}{\partial y}F_{b,\mathrm{y}}=0 \tag{24}$$

$$\frac{\partial^2}{\partial z^2}\left[h(\mathbf{P},\mathbf{T})\right]+\frac{3}{2(1+\upsilon)}\frac{\partial^2}{\partial z^2}\left(\tau_m-h(\mathbf{P},\mathbf{T})\right)+\frac{1}{2}\nabla^2\left(\tau_{zz}-h(\mathbf{P},\mathbf{T})-\frac{3\upsilon}{1+\upsilon}\left(\tau_m-h(\mathbf{P},\mathbf{T})\right)\right)+\frac{\partial}{\partial z}F_{b,\mathrm{z}}=0 \tag{25}$$

Consider the y-component of Equation 15:

$$\frac{\partial}{\partial y}\left[h(\mathbf{P},\mathbf{T})\right]+(\lambda+G)\frac{\partial}{\partial y}(\nabla\cdot\mathbf{u})+G\nabla^2 u_y+F_{b,\mathrm{y}}=0 \tag{26}$$

Differentiating Equation 26 by x, differentiating Equation 21 by y, averaging the two, and eliminating strains and displacements as before yields an equation relating the xy-shear stress component, mean stress, pore pressures, and temperatures:

$$\frac{\partial^2}{\partial x\partial y}\left[h(\mathbf{P},\mathbf{T})\right]+\frac{3}{2(1+\upsilon)}\frac{\partial^2}{\partial x\partial y}\left(\tau_m-h(\mathbf{P},\mathbf{T})\right)+\frac{1}{2}\nabla^2\tau_{xy}+\frac{1}{2}\left(\frac{\partial}{\partial x}F_{b,\mathrm{y}}+\frac{\partial}{\partial y}F_{b,\mathrm{x}}\right)=0 \tag{27}$$

Repeating this procedure for the y- and z-components of Equation 15 yields an equation for the yz-shear stress component; repeating this procedure for the x- and z-components of Equation 15 yields an equation for the xz-shear stress component:

$$\frac{\partial^2}{\partial y\partial z}\left[h(\mathbf{P},\mathbf{T})\right]+\frac{3}{2(1+\upsilon)}\frac{\partial^2}{\partial y\partial z}\left(\tau_m-h(\mathbf{P},\mathbf{T})\right)+\frac{1}{2}\nabla^2\tau_{yz}+\frac{1}{2}\left(\frac{\partial}{\partial y}F_{b,\mathrm{z}}+\frac{\partial}{\partial z}F_{b,\mathrm{y}}\right)=0 \tag{28}$$

$$\frac{\partial^2}{\partial x\partial z}\left[h(\mathbf{P},\mathbf{T})\right]+\frac{3}{2(1+\upsilon)}\frac{\partial^2}{\partial x\partial z}\left(\tau_m-h(\mathbf{P},\mathbf{T})\right)+\frac{1}{2}\nabla^2\tau_{xz}+\frac{1}{2}\left(\frac{\partial}{\partial x}F_{b,\mathrm{z}}+\frac{\partial}{\partial z}F_{b,\mathrm{x}}\right)=0 \tag{29}$$

Equations 23–25 and 27–29 relate each normal or shear stress component to mean stress, pore pressures, and temperatures, the primary variables of the mean stress geomechanical formulation.

Discretization and Solution of Simulator Equations

The fluid and heat flow and geomechanical equations are discretized in space using the integral finite difference method (Narasimhan and Witherspoon, 1976). In this method, the simulation domain is subdivided into grid blocks and those equations are integrated over a grid block volume, V:

$$\frac{d}{dt}\int_V M^k dV=\int_\Gamma \mathbf{F}^k\cdot\mathbf{n}d\Gamma+\int_V q^k dV \tag{30}$$

where Γ is the grid block surface. Because geomechanical effects result in grid block geometry changes, the integrands of Equation 25 depend on strain. This dependence is formulated as:

$$\psi(\varepsilon_\psi)=\psi_0(1-\varepsilon_\psi),\psi=A,D,orV \tag{31}$$

where subscript 0 refers to zero strain, A refers to area, D refers to distance, and V refers to volume. Replacing volume integrals with grid block volume averages and surface integrals with discrete sums over grid block surface segment averages yields the following discrete form of the simulator equations:

$$\left[M^k(1-\varepsilon_v)\right]^{i+1}-\left[M^k(1-\varepsilon_v)\right]^{i}-\frac{\Delta t}{V_0}\left[\sum_j A_0(1-\varepsilon_{\mathrm{A,j}})F_j^k+V_0(1-\varepsilon_v)q^k\right]^{i^*}=0 \tag{32}$$

where the summation is over grid block surface segments, superscript i is time step, and superscript i^* bracketing the flux and generation terms denotes that those terms are evaluated at the previous time step (i) or the current one ($i+1$).

The simulator equations and primary variables comprising the single-porosity version our formulation are summarized in Table 1. This system of equations is solved in a sequential manner using the Newton-Raphson method. The Jacobian matrices consist of square sub matrices that are associated with a grid block or a connection between two grid blocks. Conservation of mass, energy, and the mean stress equation are solved simultaneously first. Normal and shear stresses appearing in those equations are evaluated at the previous time step and the rest of the primary variables are evaluated at the current time step. Solution of those equations yields pressure, mass fractions, temperature, and mean stress at the current time step. The size of that Jacobian's sub matrices is two plus the number of mass components. The normal and shear stress equations, Equations 23–25 and 27–29, are solved next. In those solutions, pressure, mass fractions, temperature, and mean stress are evaluated at the current time step. Normal and shear stresses appearing in the Laplacian terms are also evaluated at the current time step, and other instances of those stresses are evaluated at the previous time step. The Jacobian matrix for each stress tensor component is linear, independent of the other stress tensor components, and has a sub matrix size of one. Figure 1 is a flow chart illustrating this equation solution.

Table 1—Summary of single-porosity version formulation including equations and associated primary variables for *N* mass components.

Equation	Associated Primary Variables
Conservation of mass (Eqn. 1)	Pressure, *N*-1 mass fractions
Conservation of energy (Eqn. 1)	Temperature
Mean stress (Eqn. 18)	Mean stress
Normal stresses (Eqn. 23)	xx, yy, zz normal stresses
Shear stresses (Eqn. 24)	xy, yz, xz shear stresses

Our simulator is massively parallel, with domain partitioning using the METIS and ParMETIS packages (Karypsis and Kumar, 1998; Karypsis and Kumar, 1999). Each processor computes Jacobian matrix elements for its own grid blocks and exchange of information between processors uses MPI (Message Passing Interface) and allows calculation of Jacobian matrix elements associated with inter-block connections across domain partition boundaries. The Jacobian matrix is solved in parallel using an iterative linear solver from the Aztec package (Tuminaro *et al.* 1999).

Example Problems

We provide three example problems for verification of our technique. The first is a comparison of simulation to the analytical solution for displacement caused by a uniform load on a semi-infinite elastic medium. There is no fluid or heat flow in this problem. The second is a comparison of simulation to the analytical solution for the two-dimensional Mandel-Cryer effect. The last, a single-phase depletion problem, shows a comparison of our simulation to published results.

Displacement from Uniform Load on Semi-infinite Elastic Medium

Given a semi-infinite elastic medium, the displacement caused by a uniform load acting on its surface over a circular area of radius a is given by Timoshenko and Goodier (1951) as:

$$w(r) = \frac{4\left(1-\nu^2\right)pr}{\pi E}\left[\int_0^{\frac{\pi}{2}} \sqrt{1-\frac{r^2}{a^2}\sin^2\theta d\theta}\right], r < a \tag{33}$$

$$w(r) = \frac{4\left(1-\nu^2\right)pr}{\pi E}\left[\int_0^{\frac{\pi}{2}} \sqrt{1-\frac{a^2}{r^2}\sin^2\theta d\theta} - \left(1-\frac{a^2}{r^2}\right)\int_0^{\frac{\pi}{2}} \frac{d\theta}{\sqrt{1-\frac{a^2}{r^2}\sin^2\theta}}\right], r > a$$

where p is the load, $w(r)$ is displacement at a radius r from the center of the circle, and the integrals in the brackets are elliptic integrals of the first and second kind. The normal z-direction stress along the z-axis at the center of the circle is given as well:

$$\tau_{zz} = p\left[-1 + \frac{z^3}{\left(a^2+z^2\right)^{\frac{3}{2}}}\right] \tag{34}$$

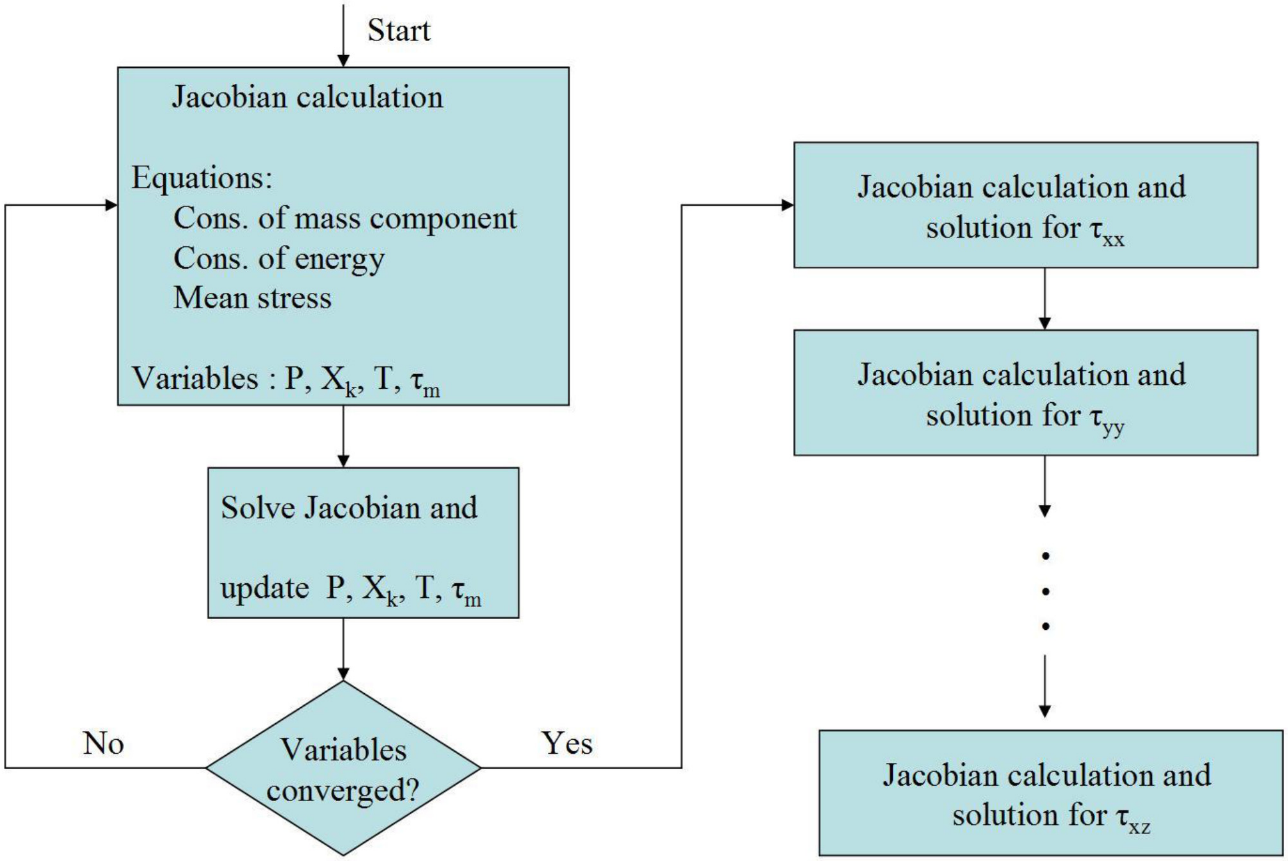

Figure 1—Flow chart for solution of mass, energy, and geomechanical equations.

We used this analytical solution to verify calculation of normal stress tensor components. We approximated the semi-infinite medium as a large rectangular parallelepiped 194 m in the x- and y-directions and 1320 m in the z-direction. We subdivided this medium into a 200x200x800 Cartesian grid. Grid block x- and y-direction length in the vicinity of the center was 0.1 m and increased further away from it. Grid block z-direction length was 0.2 m in the vicinity of the surface and increased further away from it. The loaded circle was located at the center of the top xy-face and had a 1.0 m radius. Because our grid was Cartesian, we approximated this circle as 314 loaded squares of radius 0.1 m, as shown in Figure 2. The rest of the medium's surface had no load exerted on it.

Our geomechanical formulation requires boundary conditions for mean stress and those stress tensor components that are calculated. We specified a mean stress of 0.48 MPa and a normal z-direction stress (the load) of 0.6 MPa over the loaded circle. The equal x- and y-direction normal stresses were then 0.42 MPa. There is no fluid or heat flow in this problem, so only mean stress and stress tensor components are solved for. We solve for mean stress first, and calculate stress tensor components next using the mean stress solution. Because grid block geometry depends on stress tensor components that are evaluated at the previous time step, we must repeat these calculations over a number time steps, until the stress tensor components are converged. This converged solution is that obtained by a fully coupled or fully implicit solution to these stress equations.

The displacement caused by the load is the change of the medium's overall length in the direction of the applied load, given by:

$$w = \sum D_{0,z} \varepsilon_{zz} \tag{35}$$

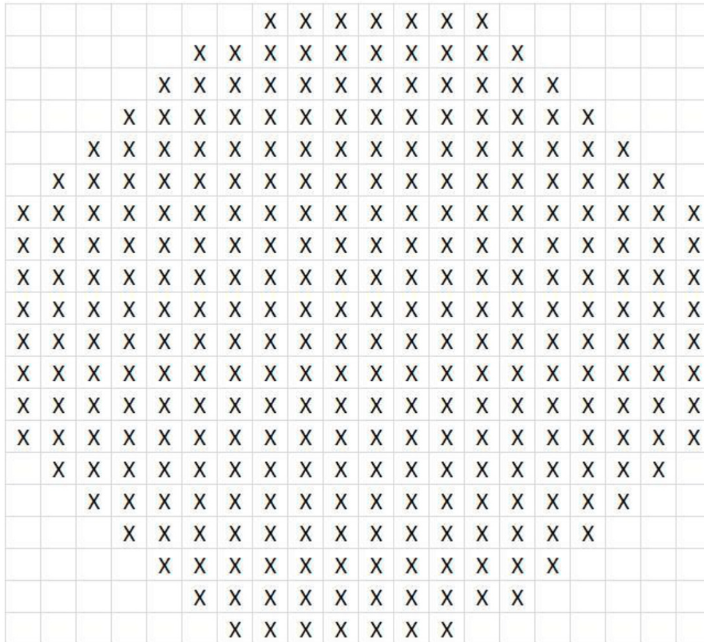

Figure 2—Approximation of loaded 1.0 m radius circle by 314 square grid blocks of length 0.1 m.

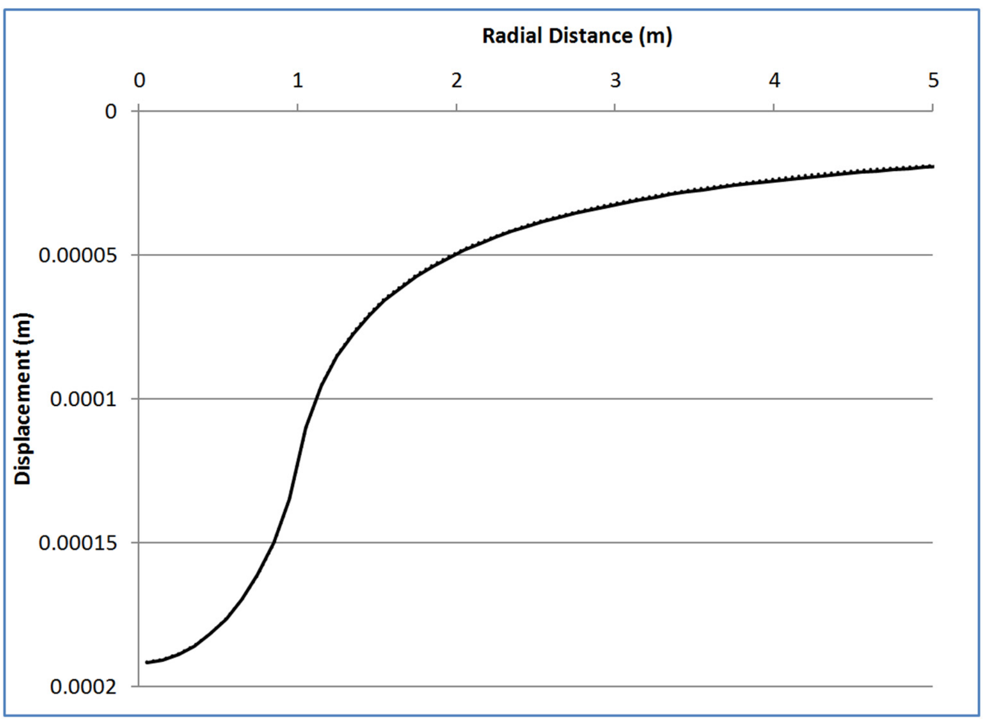

Figure 3—Analytical (solid line) and simulated (dotted line) displacements for semi-infinite medium subjected to circular load.

where $D_{0,z}$ is z-direction grid block unstrained length and the sum is over a z-direction column of grid blocks. The z-direction normal strain is calculated from Hooke's law:

$$\varepsilon_{zz} = \frac{1}{E}\left(\tau_{zz} - \upsilon\left(\tau_{xx} + \tau_{yy}\right)\right) \tag{36}$$

The analytical and simulated displacements are shown in Figure 3 and those for the z-direction normal stresses are shown in Figure 4. In both cases, they are hardly distinguishable.

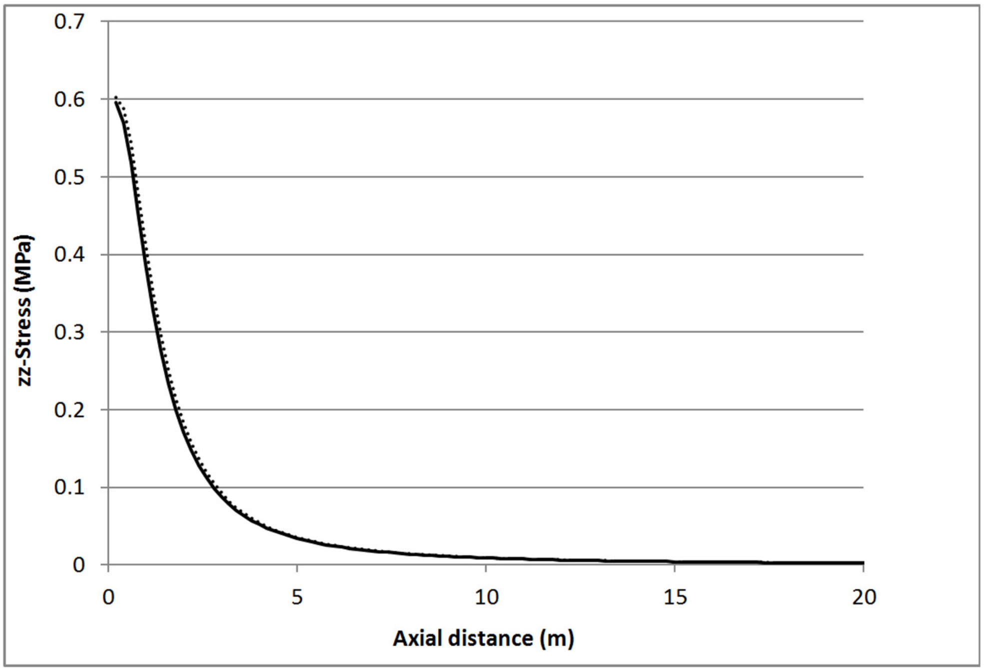

Figure 4—Analytical (solid line) and simulated (dotted line) z-direction normal stresses for semi-infinite medium subjected to circular load.

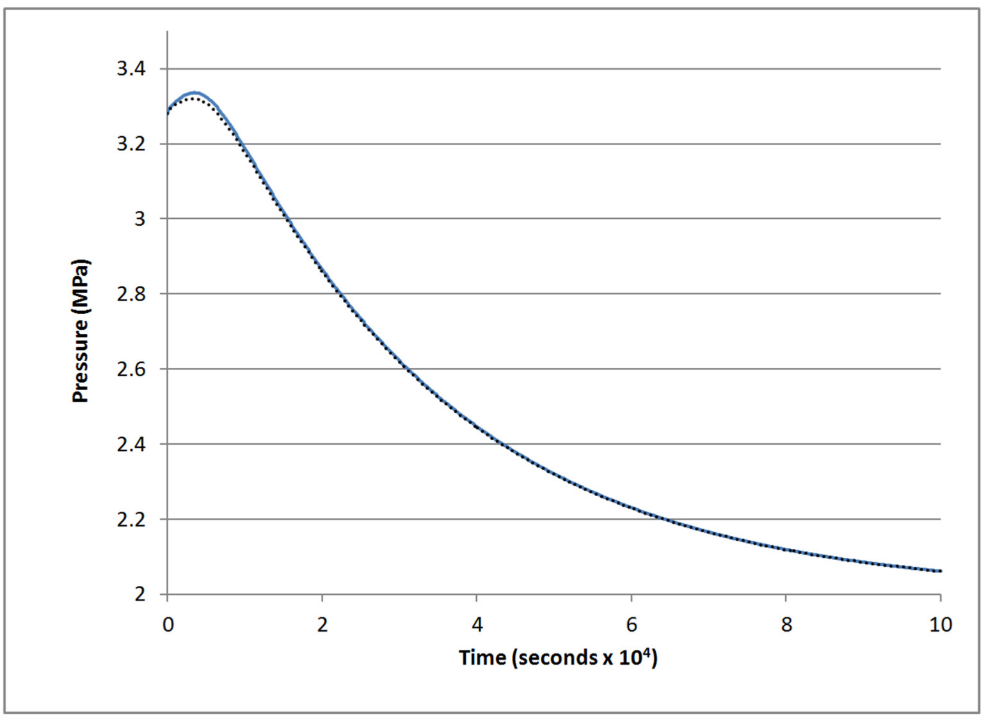

Figure 5—Match of simulated centerline pore pressure (dotted line) with analytical solution (solid line) for Mandel-Cryer effect.

Two-Dimensional Mandel-Cryer Effect

Consider a fluid-filled poroelastic material with a constant compressive force applied to the top and bottom. There is an instantaneous compression and uniform pore pressure increase due to the force. Afterwards, the material is allowed to drain laterally. Drainage is accompanied by a decrease in pore pressure near the edges and the material there becomes less stiff, resulting in a load transfer to the center and a pore pressure there that reaches a maximum and then declines. This pore pressure behavior is the

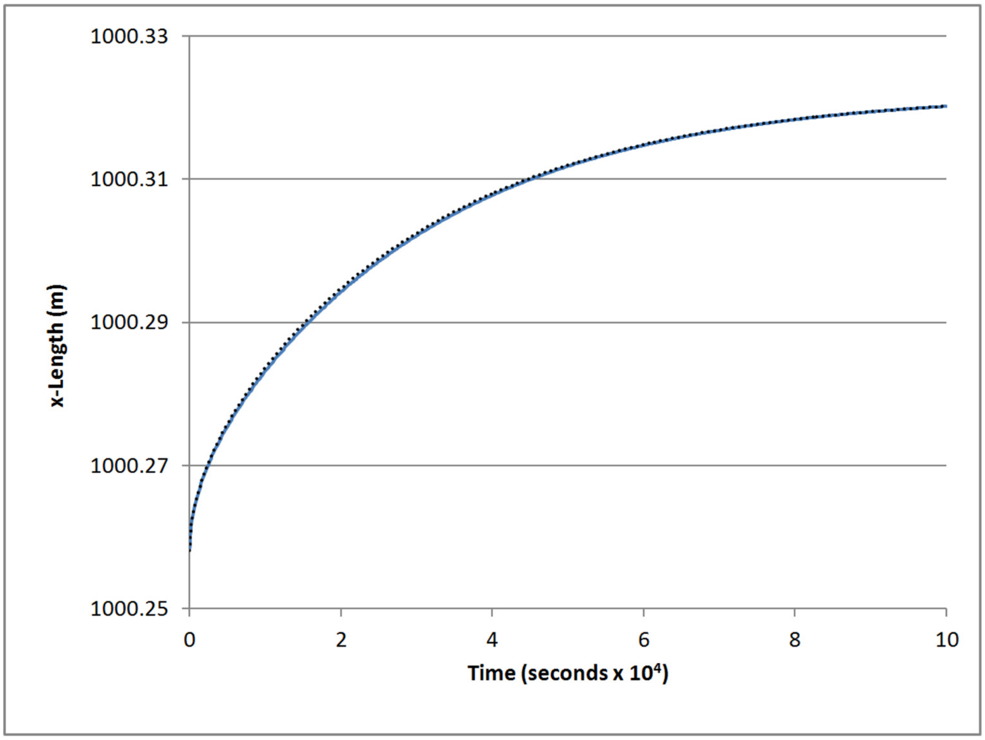

Figure 6—Match of simulated x-direction displacement (dotted line) with analytical solution (solid line) for Mandel-Cryer effect.

Mandel-Cryer effect (Mandel, 1953) and Abousleiman *et al.* (1996) derived an analytical solution to it. We use this analytical solution to verify our coupled fluid flow and geomechanics calculations.

Our simulation domain is 1000 m square and is subdivided into a uniform Cartesian 200x200 grid. Rock properties are the following: porosity is 0.094, permeability is 10^{-13} m^2, Young's modulus is 5.0 GPa, Poisson's ratio is 0.25, and Biot's coefficient is 1.0.

We simulate the compression and then the drainage. The initial unstrained state is pore pressure and normal stress components at 2.0 MPa. The compressive portion of the simulation, with an imposed mean stress of 5.0 MPa at the top and bottom, is run until equilibrium is reached. The pore pressure increases to 3.28 MPa in this step and the mean stress becomes a uniform 5.0 MPa throughout the simulation domain. Because the lateral boundaries are free, the x- and y-direction effective stresses are zero, so the normal stresses in those directions are 3.28 MPa, and the normal z-direction stress is therefore 8.44 MPa.

In the drainage portion of the simulation, the initial pore pressure (2.0 MPa) is imposed at the lateral boundaries. Because the effective stresses there are zero, the x- and y-direction normal stresses there have that value. The normal z-direction stresses at the top and bottom remain at 8.44 MPa. The drainage simulation is run for 100,000 seconds with 100 second time steps. Figure 5 shows the match of centerline pore pressure with the analytical solution. The displacements in the x- and z- directions are calculated as was done in the previous example problem. The applied stress causes the system to contract in the z-direction and expand in the x-direction. The expansion, shown in Figure 6, is matched almost perfectly and the match of the contraction, shown in Figure 7, shows only a small deviation from the analytical solution at early times.

Depletion of a Single-Phase Reservoir

We ran the depletion of a single-phase reservoir, adapted from Dean *et al.* (2006), as a comparison of our simulator to published results. A single phase (water) reservoir, 671 m^2 in area and 61 m thick, with a single vertical well at the center and completed along the entire thickness, was produced at a constant rate

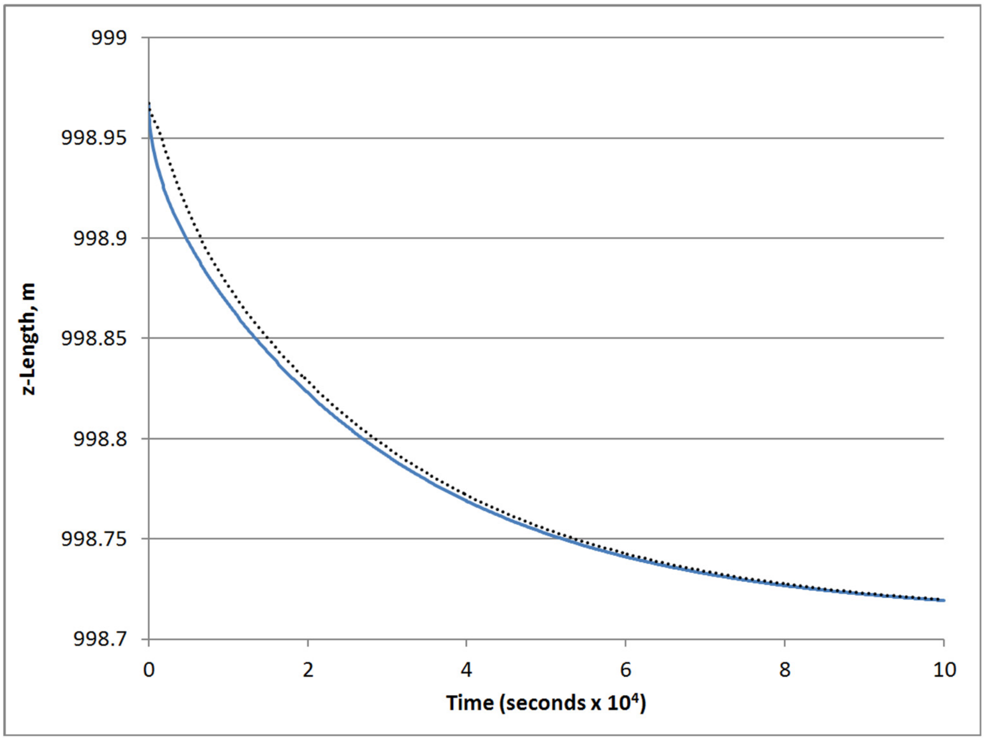

Figure 7—Match of simulated z-direction displacement (dotted line) with analytical solution (solid line) for Mandel-Cryer effect.

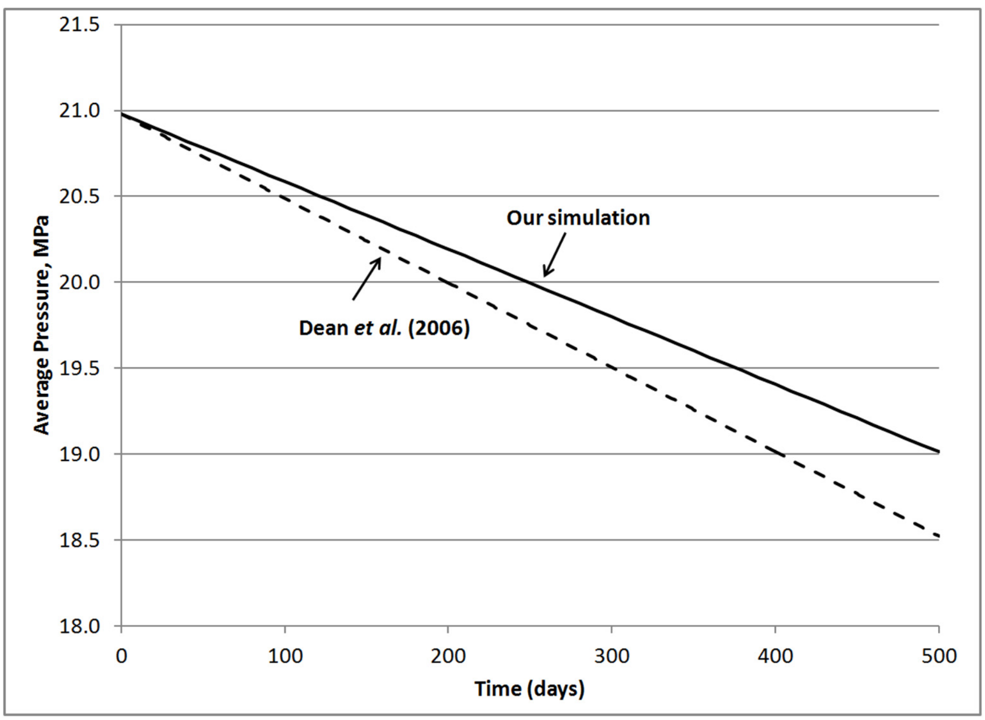

Figure 8—Average pore pressure from our simulation compared to Dean *et al.* (2006).

of 27.59 kg/sec for 500 days. Reservoir porosity was initially 0.20, horizontal permeability was $5{\cdot}10^{-14}$ m^2, vertical permeability was $5{\cdot}10^{-15}$ m^2, Young's modulus was $6.87{\cdot}10^7$ Pa, Poisson's ratio was 0.30, and the rock density was 2700 kg/m^3. The z-direction stress at the reservoir top was 41.4 MPa, and the constant horizontal stresses were 27.6 MPa. Pore pressure at the reservoir top was 20.7 MPa. Pore pressure

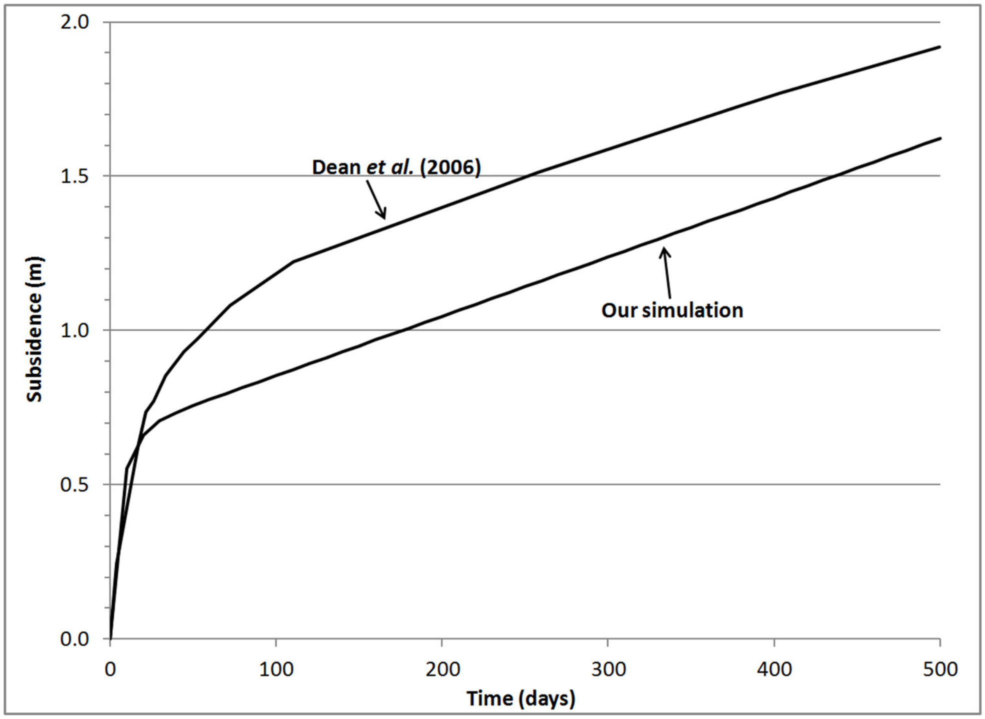

Figure 9—Subsidence from our simulation compared to Dean *et al.* (2006).

increased with increasing depth due to the hydrostatic gradient, and z-direction stress increased with increasing depth due to the overburden.

Our Cartesian grid was 11x11x10 with constant grid block dimensions, and our time step size was 50 days. Porosity varied with effective stress according to Equation 20 and solid volume was constant. Figure 8 shows a comparison of average reservoir pressure, and Figure 9 shows a comparison of subsidence around the well, between our simulation and Dean *et al.* (2006). The pore pressures at 500 days are similar but ours lies above the published results. One contributor to that is our use of a compressible fluid versus an incompressible one used by Dean *et al.* (2006). Our subsidence is also similar to the published results, and is about 16 percent less at 500 days.

Summary and Conclusions

We developed a reservoir simulator for modeling THM processes in fractured and porous media. The simulator geomechanical formulation consists of a momentum conservation equation for mean stress, pore pressures, and temperatures, along with additional equations relating each stress tensor component to mean stress, pore pressures, and temperatures. The fluid and heat flow formulation is for general multiphase, multicomponent, multi-porosity systems. The simulator is an extension of a THM one whose geomechanical formulation was the momentum conservation equation for mean stress alone.

We verified our technique using analytical solutions and published results. For the analytical solutions, we matched the displacement from a uniform load on semi-infinite elastic medium and the two-dimensional Mandel-Cryer effect. Both analytical solutions were matched by simulation extremely well, verifying the technique for calculating stress tensor components. We also ran a simulation, published in the literature, of single-phase depletion of a reservoir. The results from our simulation, namely average pressure and subsidence versus time, were similar to the published results.

Acknowledgement

This work was supported by the Foundation CMG, the EMG of the Colorado School of Mines, and by the National Energy Technology Laboratory of the U. S. Department of Energy.

Nomenclature

a	= radius, m
A	= area, L^2, m^2
C	= specific heat, L^2/t^2T, J/kg-K
D	= distance, L, m
$\boldsymbol{F}$	= mass flux, m/L^2t, kg/m^2-s
$\boldsymbol{F}_{\mathbf{adv}}$	= advective mass flux, m/L^2t, kg/m^2-s
$\boldsymbol{F}_{\mathbf{b}}$	= body force, mL/t^2, $kg\text{-}m/s^2$
$\boldsymbol{g}$	= gravity vector, L/t^2, m/s^2
G	= shear modulus, m/Lt^2, Pa
h	= specific enthalpy, L^2/t^2, J/kg
$\boldsymbol{I}$	= identity matrix
k	= permeability, L^2, m^2
k_r	= relative permeability
k_t	= thermal conductivity, mL/t^3T, J/m-s-K
K	= bulk modulus, m/Lt^2, Pa
K_s	= solid modulus, m/Lt^2, Pa
K_*	= solid modulus without fractures, m/Lt^2, Pa
M	= mass per unit volume, m/L^3, kg/m^3
M^{N+1}	= energy per unit volume, m/Lt^2, J/m^3
p	= load, m/Lt^2, Pa
P	= pressure, m/Lt^2, Pa
P_c	= capillary pressure, m/Lt^2, Pa
q	= mass source/sink per unit volume, m/L^3t, kg/m^3-s
S	= saturation
t	= time, t, s
T	= temperature, T, K
T_{ref}	= reference temperature, T, K
$\boldsymbol{u}$	= displacement vector, L, m
U	= specific internal energy, L^2/t^2, J/kg
V	= bulk volume, L^3, m^3
V_s	= solid volume, L^3, m^3
w	= displacement, m
X	= mass fraction

Greek

α	= Biot's coefficient
β	= linear thermal expansion coefficient, 1/T, 1/K
$\boldsymbol{\varepsilon}$	= strain tensor
ε_v	= volumetric strain
λ	= Lamé parameter, m/Lt^2, Pa
μ	= viscosity, m/Lt, Pa-s
ν	= Poisson's ratio

ρ = density, m/L^3, kg/m^3
$\boldsymbol{\tau}$ = stress tensor, m/Lt^2, Pa
τ_m = mean stress, m/Lt^2, Pa
τ' = effective stress, m/Lt^2, Pa
ϕ = porosity
ω = volume fraction

Subscripts

l = phase
r = rock
0 = unstrained

Superscripts

i = time step
k = mass component

References

Abousleiman Y., Cheng, A. H.-D., Cui L., Detournay, E., and Roegiers 1996. J.-C.: Mandel's Problem Revisited. *Géotechnique* **46** (2): 187–195.

Bai, M., Elsworth, D., and Roegiers, J.-C. 1993. Modeling of Naturally Fractured Reservoirs Using Deformation Dependent Flow Mechanism. *Int. J. Rock Mech. Min. Sci. and Geomech. Abstr.* **30** (7): 1185–1191.

Biot, M.A. and Willis, D.G. 1957. The Elastic Coefficients of the Theory of Consolidation. *J. Appl. Mech.* **24**: 594–601.

Chin, L.Y., Raghavan, R., and Thomas, L.K. 2000. Fully Coupled Geomechanics and Fluid-flow Analysis of Wells with Stress-dependent Permeability. *SPE Journal* **5** (1): 32–45.

Dean, R. H., Gai, X., Stone, C. M., and Minkoff, S. E. 2006. A Comparison of Techniques for Coupling Porous Flow and Geomechanics. *SPE Journal,* March, 132–140.

Gutierrez, M. and Lewis, R. W. 1996. The Role of Geomechanics in Reservoir Simulation. Presented at SPE/ISRM Eurock'96, Trondheim, Norway, 8-10 July. SPE/ISRM 47392.

Hu, L., Winterfeld, P. H., Fakcharoenphol, P., and Wu, Y.-S. 2013. A Novel Fully-coupled Flow and Geomechanics Model in Enhanced Geothermal Reservoirs. *Journal of Petroleum Science and Engineering,* **107**: 1–11.

Jaeger, J. C., Cook, N. G. W., and Zimmerman, R. W. 2007. *Fundamentals of Rock Mechanics*. Malden, MA: Blackwell Publishing.

Karypis, G. and Kumar, V. 1998. A Parallel Algorithm for Multilevel Graph Partitioning and Sparse Matrix Ordering. *Journal of Parallel and Distributed Computing* **48**: 71–85.

Karypis, G. and Kumar, V. 1999. A Fast and High Quality Multilevel Scheme for Partitioning Irregular Graphs. *Siam J. Sci. Comput.* **20** (1): 359–392.

Minkoff, S. E., Stone, C. M., Arguello, J., G., Bryant, S., Eaton, J., Peszynska, M., and Wheeler, M. 1999. Staggered in Time Coupling of Reservoir Flow Simulation and Geomechanical Deformation: Step 1 — One-way Coupling. Presented at 1999 SPE Reservoir Simulation Symposium, Houston, TX, Feburary 14-17. SPE 51920.

McTigue, D.F. 1986. Thermoelastic Response of Fluid-saturated Porous Rock. *Journal of Geophysical Research* **91** (9): 9533–9542.

Narasimhan, T. N. and Witherspoon, P. A. 1976. An Integrated Finite Difference Method for Analysis of Fluid Flow in Porous Media. *Water Resources Res.* **12**: 57–64.

Pruess, K., Oldenburg, C., and Moridis G. 1999. *TOUGH2 User's Guide, Version 2.0*. Report LBNL-43134, Lawrence Berkeley National Laboratory, Berkeley, California.

Settari, A. and Walters, D. A. 1999. Advances in Coupled Geomechanical and Reservoir Modeling with Applications to Reservoir Compaction. Presented at the 1999 SPE Reservoir Simulation Symposium, Houston, TX, February 14-17. SPE 51927.

Timoshenko, S. and Goodier, J. N. 1951. *Theory of Elasticity*. New York, NY: McGraw-Hill Book Company, Inc.

Tran, D., Nghiem, L., and Buchanan, L. 2005. Improved Iterative Coupling of Geomechanics with Reservoir Simulation. Presented at the 2005 SPE Reservoir Simulation Symposium, Houston, TX, January 31 - February 5. SPE 93244.

Tuminaro, R.S., Heroux, M., Hutchinson, S.A. and Shadid, J.N. 1999. *Official Aztec User's Guide Version 2.1*. Massively parallel computing research laboratory, Sandia National Laboratories, Albuquerque, New Mexico.

Wilson, R.K. and Aifantis, E.C. 1982. On the Theory of Consolidation with Double Porosity. *Int. J. Eng. Sci.* **20** (9): 1009–1035.

Winterfeld P. H. and Wu Y.-S. 2014. Simulation of CO2 Sequestration in Brine Aquifers with Geomechanical Coupling. In *Computational Models for CO2 Sequestration and Compressed Air Energy Storage,* edited by J. Bundschuh and R. Al-Khoury, Chapter 8, pp. 275–303, New York, NY: CRC Press.